Engineering Structures 366 (2026) 123272

Contents lists available at ScienceDirect

Engineering Structures

journal homepage: www.elsevier.com/locate/engstruct

Ultimate load performance of tubular composite joints under various loading conditions

Mathieu Koetsier [a], Gisele Cintra [a,b], Marko Pavlovic [a,*]

[a] Faculty of Civil Engineering and Geoscience, Technical University Delft, 2600 AA, Delft, The Netherlands

[b] Department of Structures and Foundations, State University of Rio de Janeiro (UERJ), Maracanã, Rio de Janeiro - RJ, 20550-013, Brazil

ARTICLE INFO

Keywords:
Interface debonding
Tubular composite joints
Ultimate load capacity
Experimental testing
Offshore structures
Cohesive zone model

ABSTRACT

This research investigates non-welded tubular composite joints, highlighting their potential for offshore structures such as wind turbine support jackets. These joints are subjected to complex loading from wind, waves, and tides, which simultaneously generate axial forces and bending moments. Tubular composite joints rely on the interfacial bond between the composite wrap and the Circular Hollow Section (CHS) members for efficient load transfer, with interfacial debonding and substrate debonding at the steel–composite boundary being the critical failure modes. This paper characterises the resistance of tubular composite joints against interfacial debonding through monotonic experiments. Hand-laminated glass-fibre-wrapped X90-joints, with chord and brace consisting of $\phi\,168.3 \times 12.5\,\mathrm{mm}$ CHS members ($\beta = 1.0$ and $d/t \approx 14$), are subjected to axial tension (N_x), axial tension combined with out-of-plane bending ($\mathrm{N}_x + \mathrm{M}_{\mathrm{op}}$), axial compression combined with out-of-plane bending ($-\mathrm{N}_x + \mathrm{M}_{\mathrm{op}}$), axial tension combined with in-plane bending ($\mathrm{N}_x + \mathrm{M}_{\mathrm{ip}}$), and axial tension combined with both out-of-plane and in-plane bending (N_x+M_{op}+M_{ip}). A total of 12 specimens were tested. The experimental programme is complemented by numerical models employing cohesive zone modelling (CZM) to predict debonding failure. The results show that debonding is the predominant failure mode across all loading conditions. Combined loading influences the sequence and extent of debonding propagation but does not alter the primary failure mechanism. An interaction equation is proposed, combining a linear interaction between N_x and the resultant bending moment with a quadratic interaction between M_{op} and M_{ip}, achieving a predictive accuracy within 10%.

1. Introduction

Steel tubular circular hollow section (CHS) joints are widely employed in engineering structures due to their favourable mechanical properties and cost efficiency [1]. Traditionally, these connections are fabricated by welding brace sections to chord members. However, in structures exposed to cyclic loading, such as bridges and offshore platforms, fatigue becomes a critical concern, particularly in weld zones where stress concentrations significantly reduce fatigue life. Offshore joints located in splash zones face additional challenges from harsh environmental conditions and repeated loading, further diminishing fatigue strength [2]. To enhance static resistance, various strengthening measures—such as can and stub attachments, doublers, local thickening, and weld-detail improvements—have been widely investigated. These techniques primarily aim to increase local stiffness and redistribute stresses away from the weld toe, thereby delaying local yielding and improving ultimate capacity. Several studies have reported substantial gains in static strength for reinforced X- and K-joints, particularly when stiffening elements are designed to reduce chord ovalisation and mitigate high-SCF weld geometries [3–5]. Among these strategies, reinforcement using stubs and cans has been commonly implemented to improve joint performance in practice [6]. Despite these advancements, strengthened welded joints remain sensitive to geometric parameters and weld quality.

Beyond fatigue considerations, the static response of welded CHS X- and K-joints has been extensively investigated due to their structural importance in offshore and tubular steel frameworks. Load transfer primarily occurs through the brace–chord weld, where localised stress concentrations and chord wall flexibility govern overall behaviour. Numerous experimental and numerical studies have demonstrated that geometric parameters—including brace-to-chord diameter ratio, chord slenderness, and brace angle—strongly influence chord plastification, local yielding, and ultimate capacity. High β-ratios and acute brace angles typically lead to elevated SCFs and premature local failure,

* Corresponding author.
E-mail address: M.Pavlovic@tudelft.nl (M. Pavlovic).

https://doi.org/10.1016/j.engstruct.2026.123272
Received 18 March 2026; Received in revised form 4 June 2026; Accepted 24 June 2026
Available online 9 July 2026

whereas lower β values and increased wall thickness promote more global and ductile chord deformation [7–10].

A novel solution proposed by TU Delft aims to eliminate the need for welding in CHS connections by utilising a glass fibre composite to connect the tubular sections [11]. This method effectively mitigates the need for additional reinforcement in fatigue-sensitive areas, offering a promising alternative to traditional welded joints.

Recent studies on the fatigue performance of these tubular composite joints have demonstrated significant improvements, with lifetime increases ranging from 10 to 5000 times compared to welded counterparts [12,13]. This considerable enhancement highlights the potential of tubular composite CHS joints for applications in structures, where current welded joint designs are primarily limited by fatigue life. However, while fatigue performance is crucial for long-term durability, the ultimate load performance of these joints under extreme loading conditions is also a critical factor. Offshore structures, such as wind turbine support jackets, are subjected to complex loading conditions, including wind, wave, and tidal forces, which generate combined load-cases in the joints. These complex loads further complicate the joint behaviour and necessitate a comprehensive understanding of the joint's ultimate load performance.

Current research has primarily focused on the failure modes and joint behaviour under uniaxial loading conditions, such as monotonic axial tension, axial compression, and in-plane bending. These studies have demonstrated that tubular composite joints offer improved stiffness and static resistance compared to their welded counterparts [14]. However, in real-world applications, these basic loading conditions rarely occur in isolation. Instead, the interaction between axial and bending loads plays a significant role in joint performance and must be considered to obtain a more comprehensive understanding of how tubular composite joints behave under complex loading scenarios.

For welded CHS joints, the interaction between axial force and bending has been widely studied. Hoadley and Yura [15,16] showed that for X-joints with $\beta = 1.0$, axial force and out-of-plane bending interact almost linearly, while Makino [17] reported similar behaviour in T-joints. At lower β values, saddle stiffness decreases, leading to more distributed load transfer [18]. In contrast, axial force and in-plane bending show a near-quadratic interaction, since axial loads are resisted mainly in the saddle region and in-plane bending in the crown regions, with little overlap between the two.

The interaction equation Eq. (1), originally proposed by Hoadley and Yura [15], forms the basis for CHS joint design and is adopted in Eurocode [19], DNV [20], NORSOK [21], and CIDECT [22]. However, tubular composite joints rely on bonding rather than welding, so their load transfer mechanisms differ and require dedicated investigation.

$$\frac{N_x}{N_{x_u}} + \left|\frac{M_{op}}{M_{op_u}}\right| + \left(\frac{M_{ip}}{M_{ip_u}}\right)^2 = 1 \tag{1}$$

- N_x : Applied axial force in the joint (in kN).
- N_{x_u} : Ultimate axial capacity of the joint under pure axial loading.
- M_{op} : Applied out-of-plane bending moment (in kN m).
- M_{op_u} : Ultimate capacity of the joint under pure out-of-plane bending.
- M_{ip} : Applied in-plane bending moment (in kN m).
- M_{ip_u} : Ultimate capacity of the joint under pure in-plane bending.

This paper presents experimental results on medium-scale 90° tubular composite X-joints with a CHS diameter of ø168.3 × 12.5 mm. The joints were subjected to a variety of loading configurations, including monotonic uniaxial tension N_x, combined axial tension with out-of-plane $\mathrm{N}_x + \mathrm{M}_{\mathrm{op}}$ and in-plane bending $\mathrm{N}_x + \mathrm{M}_{\mathrm{ip}}$ and full multi-axial loading $\mathrm{N}_x + \mathrm{M}_{\mathrm{op}} + \mathrm{M}_{\mathrm{ip}}$. This study utilised the TU Delft hexapod, a unique six degree of freedom (DoF) testing apparatus [23]. The study investigates the failure modes and their interactions under these different loading conditions, with a particular focus on the influence of combined loads on deformation capacity and ductility. Complementary finite element (FE) models were utilised to enhance the interpretation of experimental trends and validate key assumptions. The results highlight the performance of the tubular composite joints, which, in some cases, exceed the yield resistance of the uncovered CHS, with debonding at the steel-FRP interface emerging as the primary failure mode. Based on the experimental results, the interaction equation for welded joints has been modified to suit the unique characteristics of tubular composite joints. A detailed recommendation and rationale are presented to describe the interaction between axial force and bending moments, highlighting their combined influence on joint resistance under multi-axial loading conditions. The presented findings demonstrate the exceptional strength, deformation capacity, and durability of the composite joints, even under complex multi-axial loading conditions. Notably, the joints exhibit capacities that approach or exceed the plastic yield resistance of the connected CHS members, highlighting the effectiveness of the composite in enhancing joint performance.

Table 1
Mechanical properties of the composite material.
Source: Table adapted from [14].

In-plane Mechanical properties	Symbol	Average value (CoV [%])
Compressive strength	$f_{x,c} = f_{y,c}$	200 (MPa) (3.79)
Compressive modulus	$E_{x,c} = E_{y,c}$	12 077 (MPa) (4.50)
Tensile strength	$f_{x,t} = f_{y,t}$	216 (MPa) (5.78)
Tensile modulus	$E_{x,t} = E_{y,t}$	11 798 (MPa) (6.37)
Major Poisson's ratio	ν_{xy}	0.15 (6.50)
Shear strength	$f_{xy,v}$	72.2 (MPa) (2.59)
Shear modulus	G_{xy}	3120 (MPa) (6.81)

2. Experimental setup and procedure

2.1. Specimen design and production

The medium-scale 90° tubular composite X-joints, depicted in Fig. 2(a), represent an innovative design method for tubular composite connections. The design concept involves the application of composite material directly around the steel CHS, eliminating the need for welding and the use of adhesives.

The medium-scale X90 joints are scaled to 1/4 of a full-scale jacket design to match the test setup capacity. The design was refined to promote debonding at the steel–FRP interface as the governing failure mode. To prevent yielding, the d/t ratio was reduced from 850/20 to 168/12.5 by increasing the steel thickness from 4 mm to 12.5 mm.

Specimens consist of two ø168.3 × 12.5 mm CHS braces connected to a chord of the same dimensions ($\beta = 1.0$, S355J2H steel). Composite lengths were set to 1.5D (brace) and 1.0D (chord) to ensure debonding-dominated behaviour (see Fig. 1(a)).

The composite laminate was hand-laid using bi-directional E-glass and vinyl ester resin. It tapers from 55 mm at the root to zero at the ends, providing quasi-isotropic properties (Table 1). Before lay-up, all steel surfaces were grit-blasted to an Sq value of 20.52 μm and degreased. Specimen fabrication was carried out under consistent indoor conditions of 16–26 °C and relative humidity between 40%–70%. After lay-up, room-temperature curing was applied for a minimum of seven days. In the doubly-curved region at the brace–chord intersection, the layup achieves near-quasi-isotropic in-plane properties. In contrast, the singly-curved cylindrical brace and chord regions exhibit primarily 0°–90° fibre alignment. For strain monitoring, Ormocer®-coated optical fibres were embedded approximately 2.4 mm from the steel–FRP interface (Fig. 2(b)).

To enable loading, machined flanges were butt-welded to the brace ends.

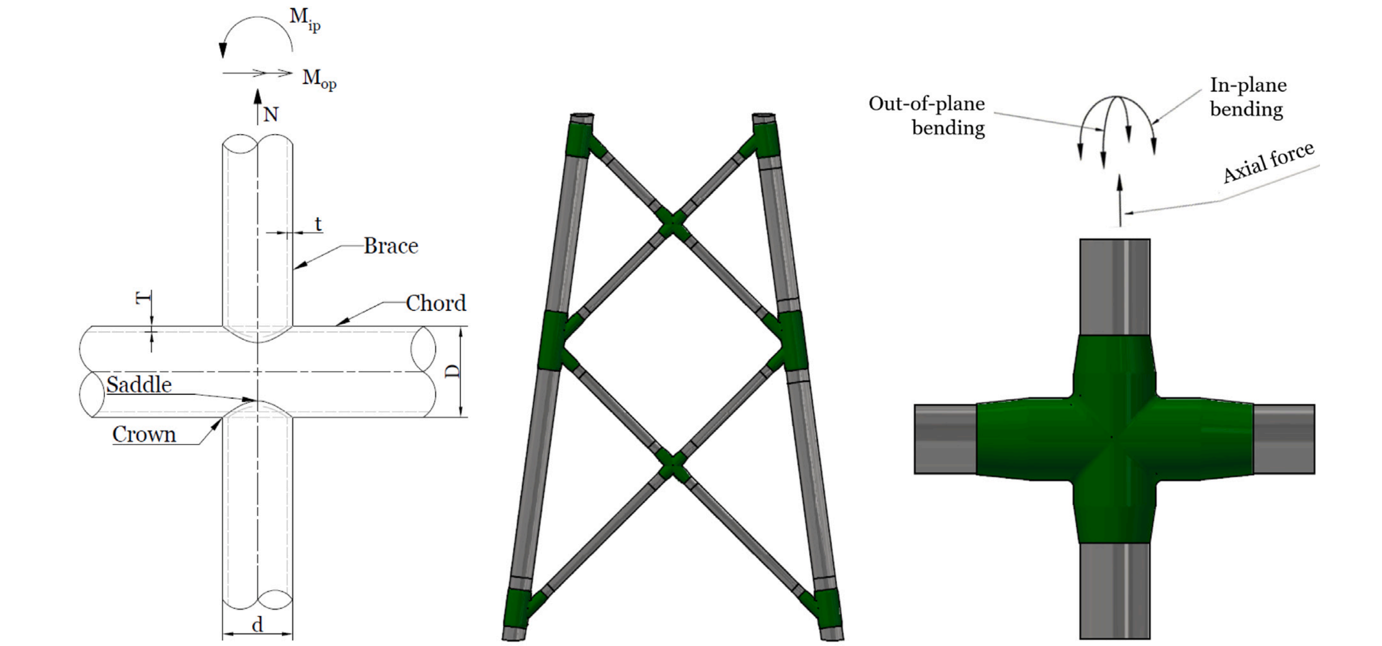

(**a**) Joint definitions (**b**) Load directions taken from [23]

Fig. 1. Joint definitions and load directions [24].

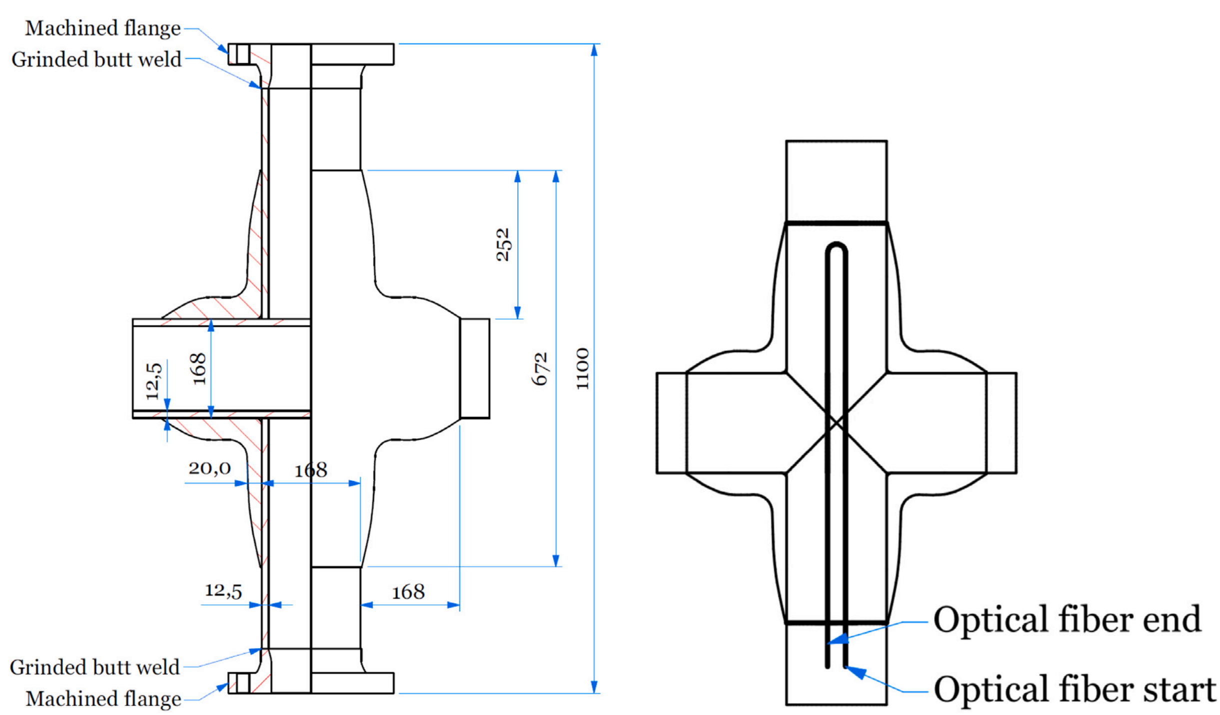

(**a**) Dimensions (**b**) Optical fibre arrangement

Fig. 2. X90 medium-scale tubular composite joint.

2.2. Loading conditions

The experimental campaign investigates six distinct loading scenarios: uniaxial tension (N_x), axial tension combined with out-of-plane bending ($N_x + M_{op}$) at three different axial-to-bending ratios, axial tension with in-plane bending ($N_x + M_{ip}$), and axial tension in conjunction with both out-of-plane and in-plane bending ($N_x + M_{op} + M_{ip}$), see Table 2. Pure bending load cases—i.e., uniaxial out-of-plane and in-plane bending—are not included in this series. Previous research [25] has shown that for the current joint configuration, the response under pure bending is governed by the plastic capacity of the CHS brace itself, independent of the composite. This indicates that the failure mode in such cases is dictated by the global yielding of the steel section rather than any interaction effects at the steel–FRP interface. As a result, the plastic bending moment of the CHS is considered the ultimate bending capacity and used as a reference in interpreting the combined loading results. The current study therefore focuses on understanding how axial tension interacts with bending moments, which more accurately reflects the complex multi-axial conditions found in practice and highlights the influence of the composite reinforcement on joint performance.

In all monotonic tests, displacement control is applied. For uniaxial loading, a single degree of freedom (DOF) is controlled, whereas in multi-axial loading scenarios, two or three DOFs are simultaneously regulated. During the uniaxial tensile test, the actuator displacement rate is set to 1.0 $\mathrm{mm\,min^{-1}}$, corresponding to an average strain rate of 1.3 $\mu\epsilon\,\mathrm{s}^{-1}$ in the brace, as measured using Digital Image Correlation (DIC). For the multi-axial cases, both translational and rotational velocities are adjusted such that the average interface strain rate remains consistent with this target value. An overview of the controlled DOFs, loading types, number of specimens, and applied loading rates is summarised in Table 2.

For the combined loading cases, the proportions between axial force and bending moments were derived from a two-fold criterion. First, a case study of an offshore jacket foundation supporting a 20 MW wind turbine in 60 m water depth was considered. Typical load ratios observed in this design were used to define realistic multi-axial scenarios, ensuring that the experimental programme reflects practical offshore conditions. Second, preliminary Finite Element (FE) models, calibrated against axial tension tests, were used to confirm that the combined load responses remain within the test system's capacity. This approach ensures that the applied loads are both theoretically justified and structurally relevant.

Based on this criterion, three specific force-to-moment ratios were selected. A ratio of 6 $\mathrm{m^{-1}}$ is adopted for $\mathrm{N}_x + \mathrm{M_{op}}$ to emphasise the role of the out-of-plane bending moment in joint failure. A ratio of 12 $\mathrm{m^{-1}}$ is applied to both $\mathrm{N}_x + \mathrm{M_{op}}$ and $\mathrm{N}_x + \mathrm{M_{ip}}$, ensuring that the axial force and bending moment contribute equally to failure. Finally, a ratio of -12 $\mathrm{m^{-1}}$ is used for $-\mathrm{N}_x + \mathrm{M_{op}}$ to investigate the joint's behaviour under combined compression and out-of-plane bending. For the complete multi-axial load case $\mathrm{N}_x + \mathrm{M_{op}} + \mathrm{M_{ip}}$, a ratio of 12 $\mathrm{m^{-1}}$ is applied for both $\frac{\mathrm{N}_x}{\mathrm{M_{op}}}$ and $\frac{\mathrm{N}_x}{\mathrm{M_{ip}}}$ to study the interaction between $\mathrm{M_{op}}$ and $\mathrm{M_{ip}}$. Together, these ratios capture the interaction effects between axial and bending loads, providing a comprehensive understanding of joint performance under realistic conditions.

To ensure uniform multi-axial loading conditions across different scenarios, the experiment maintains a fixed ratio between translation speed in the z-direction and rotation speed around the x and/or y-axis. This approach results in proportionate joint loading during the testing. The primary objective is to establish conditions favourable for inducing debonding failure while reducing plastic deformation in the steel CHS.

2.3. Test equipment and instrumentation

Two experimental setups were used: a uniaxial tensile frame and the TU Delft Hexapod for combined load cases. The tensile setup, a 6 m high frame with a 2.5 MN actuator (±50 mm stroke), allowed tests to failure under uniaxial loading (Fig. 3(a)). Specimens were mounted with hinged supports and load was measured using a 2.5 MN load cell.

For multi-axial loading, the TU Delft Hexapod [23] was employed (Fig. 4(a)). The system consists of six hydraulic actuators (±300 kN, ±300 mm stroke) arranged in pairs between a base and crosshead, providing full six-degree-of-freedom (DoF) control. Operating at up to 1500 L/min and 280 bar, it enables the application of complex proportional load paths, including combined axial, bending, and torsional components (see Table 3), with a frequency range up to 30 Hz [26]. Specimens were clamped between custom base and top plates using prestressed bolts. Forces in each actuator leg were recorded through integrated load cells and transformed into global axial forces and bending moments. The Hexapod's control software converted prescribed displacements and rotations into actuator motions, ensuring precise and repeatable loading conditions.

The campaign focused on joint performance under monotonic loading, with special attention to debonding at the steel–FRP interface. To capture both global deformation and local debonding, two complementary monitoring techniques were used: 3D Digital Image Correlation (DIC) and embedded distributed optical fibres. DIC measured global displacements and surface strains, while fibres provided high-resolution strain data near the interface, allowing synchronised tracking of debonding progression.

Two GOM ARAMIS 800 systems [27] were employed. For uniaxial tests, one system was placed on a single side; for combined loading, both sides were monitored (Fig. 5(a)). The DIC method indirectly detected debonding from surface strain patterns as shown by [14]. Additional measurement rings are mounted to the flanges to isolate specimen response and quantify six DoF motions (Fig. 5(b)). This enabled precise stiffness and rotation assessment with minimal setup influence.

Optical fibres (Fig. 2(b)) were connected to a Luna ODISI 6000 interrogator [28], achieving 0.65 mm spatial strain resolution via Rayleigh backscatter. As shown by Koetsier and Pavlovic [29], this method allows identification of interface debonding and substrate debonding along the fibre path. Feng et al. [30] have shown a good agreement of strain distributions between DIC and optical fibre measurements.

2.4. Specimen instrumentation

Before testing, each specimen undergoes a comprehensive preparation process to ensure accurate measurements and reliable results. First, a 3D scan of the untested specimen is conducted using the Artec Leo handheld scanner [31], which offers an accuracy of 0.1 mm. This scan produces a detailed digital twin of the specimen, capturing both its geometry and surface texture. These 3D models are used to compare the specimen's geometry to the CAD design and to identify any deviations between different specimens.

Next, the optical fibres embedded during production are prepared for strain measurements. At the fibre's starting point, a pigtail is spliced to establish a connection to the Luna ODISI interrogator. To enable accurate Rayleigh backscattering, any light reaching the fibre's end must be dispersed to prevent excessive backscatter and sensor oversaturation. This is achieved by splicing a core-less fibre at the end, which effectively disperses the light. Finally, the Luna ODISI software is used to create a "fingerprint", converting the optical fibre into a fully functional strain measurement sensor. All steps in the sensor preparation process are performed in-house.

For DIC measurements, the specimen surface is prepared with a speckle pattern to ensure optimal image tracking. Two layers of matte white paint are applied with a brush to create a uniform base, followed by a black speckle pattern applied using a spray method. The speckles are approximately 4 mm in size, ensuring sufficient contrast and accuracy during testing.

3. Results and analysis

This section presents the experimental results, supported by finite element (FE) modelling as a complementary tool to provide deeper insights into the observations made during the experiments. The FE modelling approach, initially developed by He et al. [32], serves as a complementary tool. To enhance the interpretation of the experimental results, particularly by providing additional insights into the debonding process under uniaxial loading conditions. This numerical model is only applied to the uniaxial tension case, as it represents the simplest boundary condition and loading path, allowing for a more direct validation of the model and clear interpretation of the failure mechanisms. For multi-axial load cases, the added complexity in load interaction and deformation paths requires further model development and calibration,

(a) Experimental setup for uniaxial tensile tests

(b) Tensile specimen

Fig. 3. Experimental setup of uni-axial tensile loading.

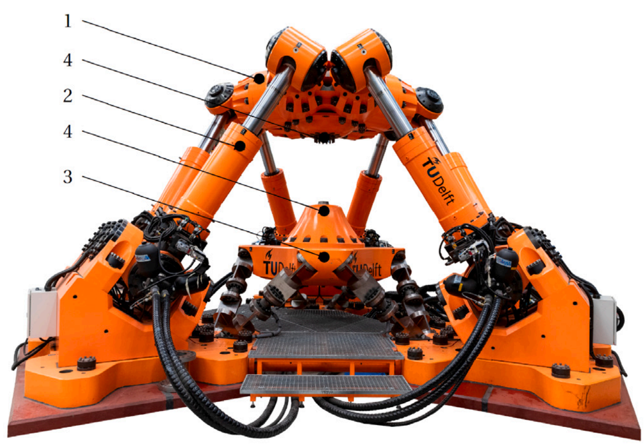

(a) TU Delft Hexapod. 1 = platform; 2 = actuator; 3 = pedestal 6 DoF loadcell; 4 = specimen grips. Figure adapted from [25].

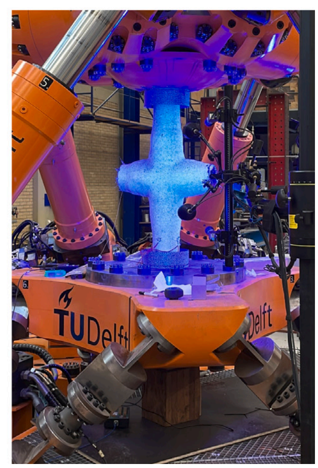

(b) Specimen placed in the TU Delft Hexapod

Fig. 4. Experimental setup of multi-axial loading.

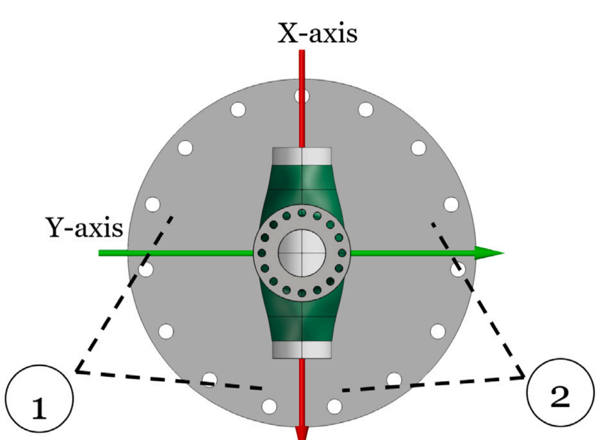

(a) DIC positions in combined loading (top view)

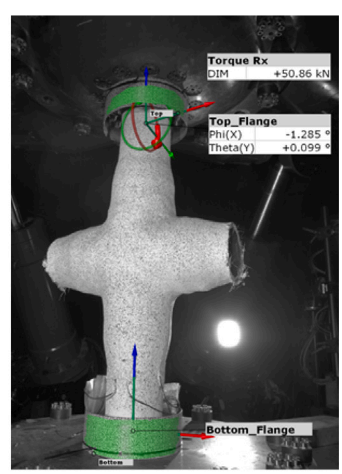

(b) Measurement rings in combined loading (side view)

Fig. 5. DIC measurement setup for combined loading.

Table 2
Overview load condition.

	N_x	$N_x + M_{op}$	$N_x + M_{op}$	$-N_x + M_{op}$	$N_x + M_{ip}$	$N_x + M_{op} + M_{ip}$
Loadcase nr.	LC1	LC2	LC3	LC4	LC5	LC6
Nr of specimens.	2	2	2	2	2	2
Specimen name	B26	B38	B36	B45	B34	B30
	B40	B44	B37	B51	B47	B31
Ratio $\frac{N}{M}$	-	6m^{-1}	12m^{-1}	-12m^{-1}	12m^{-1}	8.5m^{-1}
v_z (mm min^{-1})	1.00	0.15	0.15	0.15	0.15	0.15
ω_x (° min^{-1})	-	0.066	0.066	0.066	0.066	0.066
ω_y (° min^{-1})	-	-	-	-	-	0.066

v_z the translation velocity along the z-axis,
ω_x the angular velocity around the x-axis,
ω_y the angular velocity around the y-axis.

Table 3
TU Delft Hexapod displacement and load capacity [26].

Description	Capacity
Axial force	±1000 kN
Shear force	±400 kN
Bending moment	±400 kN m
Torsion moment	±1000 kN m
Vertical displacement	±450 mm
Lateral translation	±300 mm
Bending rotation	±11°
Torsional rotation	±20°

which falls outside the scope of this study. Additionally, the model is used to support and clarify the procedure for determining crack length from the distributed optical fibre measurements.

For each loading condition, the load–displacement response is analysed, and key observations are highlighted. This is followed by a comparative assessment of failure modes across different load cases and an evaluation of the joint's deformation capacity and ductility under various loading conditions. In this section, a comparison is also made to the design resistance of welded equivalent joints with identical geometry, where the design resistances are calculated using the formulas provided in Eurocode 1993-1-8 (2025). The uniaxial design resistances for a yield strength of 355 MPa and a material safety factor of $\gamma_{M_0} = 1.0$ are given by $N_x = 1279.5$ kN, $M_{ip} = 103.9$ kN m, and $M_{op} = 107.5$ kN m. For combined loading cases, the interaction criterion specified in Eurocode is applied. This comparison is essential because it provides a benchmark against established CHS connection methods, highlighting the potential performance advantages of composite joints over conventional welded joints.

3.1. Finite element model

The FE modelling strategy of He et al. [32] was adopted and implemented in Abaqus [33], using a dynamic explicit solver to capture nonlinear contact and interface behaviour. Details are given in [32,34]. The composite geometry was discretised with C3D4 tetrahedra (4–16 mm), while the steel brace and chord were meshed with C3D8 hexahedra (4 mm). The elements at the interface have an element size of 4 mm, increasing to 16 mm at the outer surface of the composite. These mesh densities were determined through a mesh convergence study in which three composite discretisations were compared: 2–8 mm, 4–16 mm, and 8–32 mm. The joint response remained consistent between the 2–8 mm and 4–16 mm meshes, whereas the 8–32 mm mesh produced slight deviations in the predicted load–displacement response and a loss of resolution in the interface strain field. The 4–16 mm discretisation was therefore adopted as it offers an optimal balance between accuracy and computational cost. To accurately represent the composite, 3D scan data of the specimen (Section 2.4) were processed into a watertight mesh (Artec Leo [31], VXelements [35]), combined with the steel CAD geometry (Autodesk Inventor [36]), and imported into Abaqus (Fig. 6).

The cohesive zone modelling (CZM) approach is employed to simulate debonding failure at the steel-FRP interface. The traction-separation law is applied between the outer steel surface and the inner composite surface, with the interface thickness considered negligible due to the manufacturing process. Friction, arising from composite contraction during curing and Poisson effects under loading, significantly influences the load transfer mechanism and is incorporated into the FE model via a friction coefficient assigned to the debonded area. The traction–separation law and friction coefficient are based on He et al. [34].

The comparison between experimental and numerical load–displacement responses in Fig. 7 shows strong agreement in terms of initial stiffness, onset of non-linearity, and ultimate load.

3.2. Axial tensile loading

The load–displacement response under N_x loading is shown in Fig. 7. Experimental results are compared with simulations using a previously calibrated FE model with CZM parameters from 4ENF and DCB tests [37,38]. Experimental and numerical strains were analysed at the optical fibre locations, focusing on debonding progression at points A–D. These points mark changes in strain distribution and crack growth.

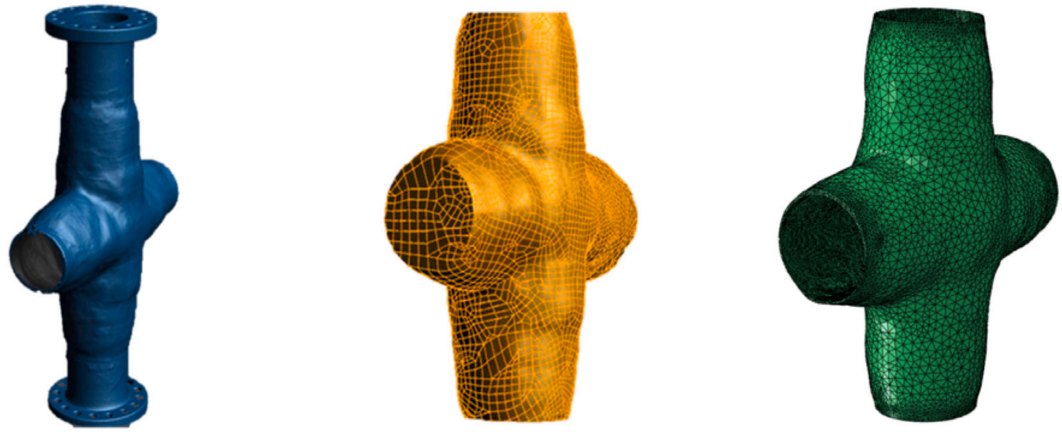

(a) 3D scanned surface **(b)** 3D solid from scanned geometry **(c)** Final FE mesh of composite

Fig. 6. Steps from 3D scan to solid in the FE model.

Strain distributions from experiments and simulations (Fig. 8) show good agreement; numerical results were scaled to match experimental force levels.

The X-joint demonstrates a quasi-ductile response, characterised by progressive interface damage with maintained load-carrying capacity, attaining an ultimate load of approximately 1700 kN at a displacement of 4 mm. This ultimate capacity of 1700 kN substantially exceeds the Eurocode design resistance of the equivalent welded joint (N_x = 1279.5 kN see Fig. 7), representing an enhancement of approximately 33%. Linear behaviour is observed up to 500 kN (point A), when debonding initiates at the crown region. Between 500–800 kN, debonding progresses at the brace–chord root. At point B (800 kN), debonding also initiates in the saddle (Fig. 9(c)), propagating into chord and brace. From B to C (1200 kN), crack growth localises in the saddle, and from C to D (1400 kN) extends towards the crown (Figs. 9(d) and 9(e)), increasing crack width and joint ductility. At D, circumferential cracking enhances resistance, after which full debonding occurs by 1700 kN. This behaviour appears typical for joints with $\beta = 1.0$.

Crack lengths were derived from fibre strains using an FE-based calibration. Strains along the fibre path were extracted and compared with FE Cohesive Surface Damage Variable (CSDMG) values (Figs. 10, 11). A threshold of 3300 $\mu\epsilon$ provided the best agreement with FE-predicted crack lengths; sensitivity to this threshold is discussed in [29]. Reliable crack length determination was achieved up to 150–200 mm, beyond which deviations arose due to geometry effects. Experimental results (joint B26) confirmed dominant crack growth between C and D, consistent with FE predictions. A 5% difference in ultimate load between experiments is attributed to hand-lamination variability.

Stress distributions from the FE model further clarify load transfer. Fig. 12 shows longitudinal stresses along the brace axis, with concentrations in the saddle region, similar to welded joints with $\beta = 1.0$ [16]. At C and D, stresses peak around the out-of-plane face, reflecting the dominant role of continuous fibres in carrying load.

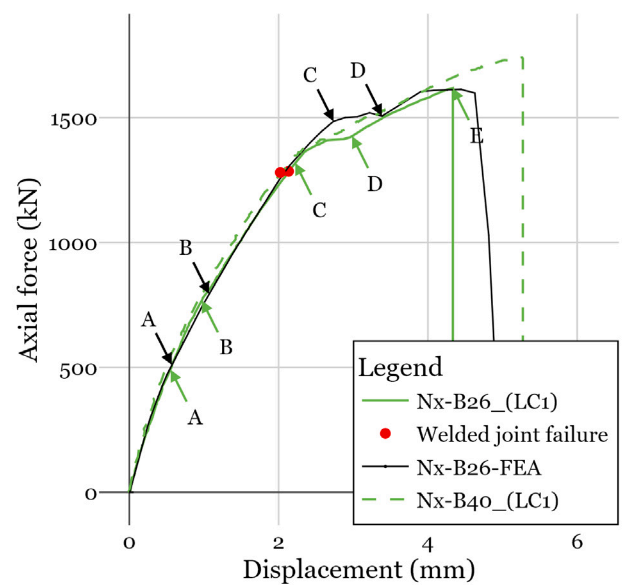

Fig. 7. Load–displacement load case N_x including predicted failure of welded joint.

3.3. Axial tension + out-of plane bending loading

Four tests were conducted to investigate the interaction between axial tensile loading and out-of-plane bending of the brace. The load–displacement response of the X-joint subjected to $N_x + M_{op}$ is analysed for both LC2 and LC3 (see Table 2). LC2 represents a bending-dominated loading condition with approximately 37% of the ultimate axial load, while LC3 corresponds to an axial-dominated condition with approximately 60% of the ultimate axial load. Each case contains two identical experiments. The experimental load–displacement results are presented in Figs. 13 and 14.

The progression of debonding is characterised by identifying key points along the force–deformation response in a similar manner as it was done for uniaxial tension loading case but without the help of FE model. Development and calibration of the FE model that covers behaviour of all multi-axial load cases is not part of the scope of this paper. Figs. 13 and 14 show similar load–displacement behaviour for LC2 ($N_x + M_{\text{op}}$ (with M dominant)) and LC3 ($N_x + M_{\text{op}}$ (with N dominant)) compared to LC1 (N_x). Points C–D and E–F are indicating the expansion of debonding towards the brace sides for the bottom and top braces, respectively. This behaviour is further validated by the strain distribution measured through embedded optical fibres. Notably, for both $N_x + M_{op}$ load cases — regardless of whether axial force or bending moment dominates — a more pronounced asymmetry in debonding progression is observed between the top and bottom braces. The observed asymmetry is likely due to larger bending moments in the bottom brace, caused by the tensile load applied at the top. As loading increases, the joint deforms laterally to accommodate bending in the absence of shear forces, introducing eccentricity in the tensile load. This reduces bending moments slightly more in the top brace than in the bottom brace.

Fig. 8. Comparison optical fibre results experiment and FE model Nx-B26. With indication of start and end of optical fibre in Fig. 2(b).

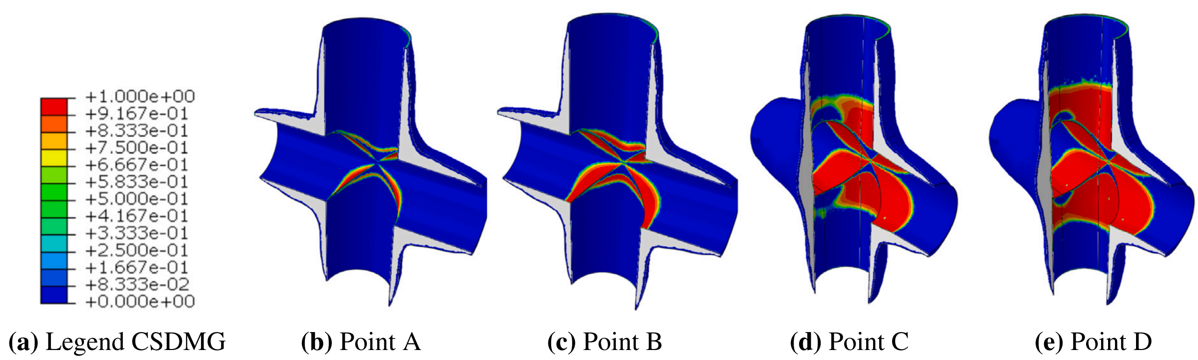

Fig. 9. Debond patterns for load-case N_x for point A to D.

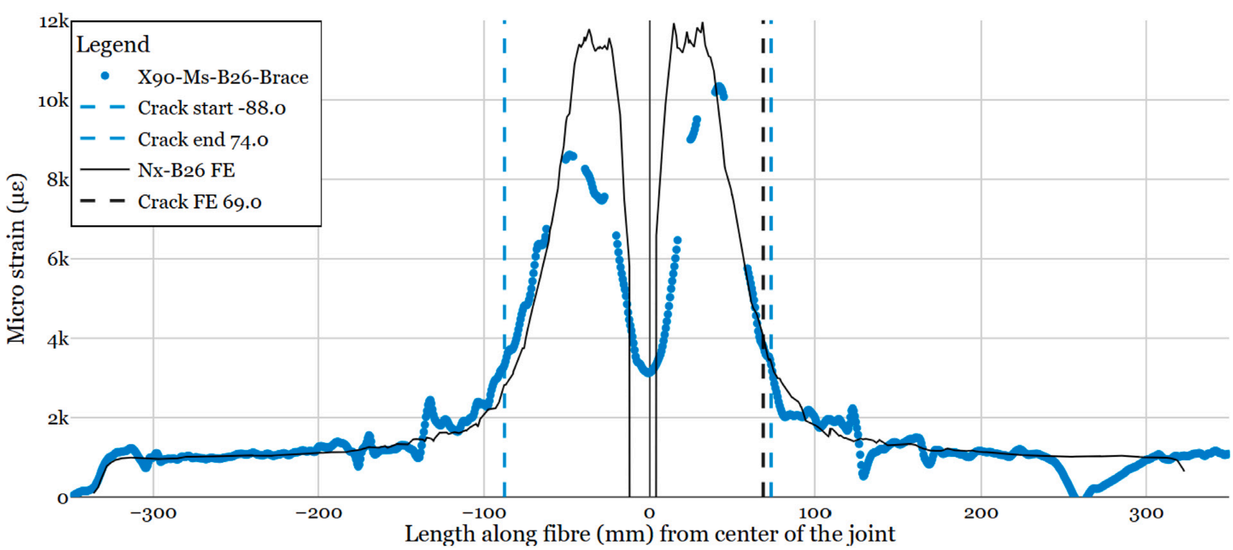

Fig. 10. Crack length derivation from optical fibre results experiment and FE model for LC1 (N_x)

The major surface strains corresponding to points C, D, E, and F are presented in Figs. 15 and 16, with these points also marked on the load–deformation curves in Fig. 14. The transition from point C to D reflects the initiation and propagation of debonding in the top brace towards the crown region. This is clearly visible in the optical fibre strain results, where the top brace is represented from 0 mm to −300 mm; the strain front progressively moves towards the end of the composite. From point D to E, the debonding continues primarily in the top brace. After point E, debonding initiates in the bottom brace and similarly advances towards the crown. This evolution is captured

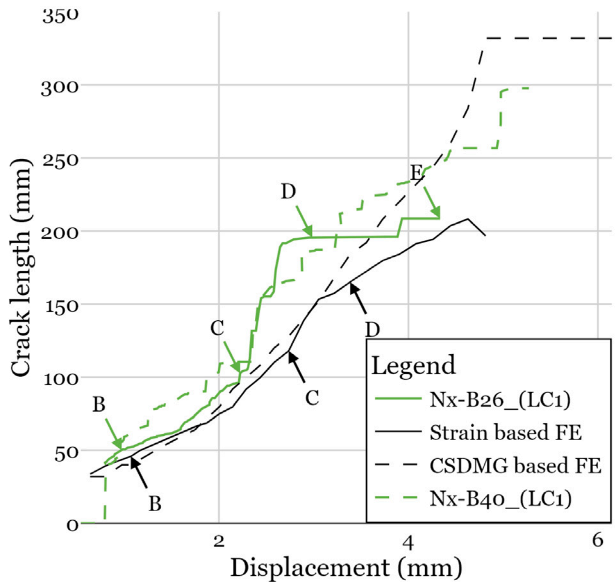

Fig. 11. Crack length load case N_x.

in both the DIC measurements and optical fibre strain profiles shown in Figs. 15 and 16, respectively. At point F, complete debonding of the bottom brace is observed. The sequence and extent of debonding seen in the DIC surface strain maps are well supported by the corresponding optical fibre measurements.

A key observation is that the bending moment reaches a plateau at point F, once debonding extends towards the brace sides, while axial resistance continues to increase. This can be attributed to steel yielding, as the bending moment resistance is more sensitive to the initiation of plastic strains at the outer parts of the cross-section compared to axial resistance. A similar response is observed for LC3 (N_x + M_{op}), where the axial force-to-bending moment ratio is higher. In this case, crack propagation towards the crown is evident in both braces. The results indicate that for LC3, the increase in bending resistance following the onset of yielding is less pronounced compared to LC2. Differences arises due to the higher axial force in LC3, which amplifies the influence of bending moment on the plastic cross-sectional area, thereby reducing the post-yield bending capacity.

3.4. Axial compression + out-of-plane bending loading

To investigate the interaction between axial compression and out-of-plane bending in the brace, two tests were performed on X-joint specimens subjected to the $-N_x$ + M_{op} loading condition. This scenario, represented by load case LC4 in Table 2, reflects a compression-dominated load combined with out-of-plane bending. The resulting load–displacement response is shown in Fig. 17.

Experimental observations using distributed optical fibre sensors and DIC revealed no signs of debonding for this load case. This absence of damage is attributed to two mechanisms acting in combination. First, under axial compression, the brace is pressed directly against the chord, allowing a significant portion of the axial load to be transferred through steel-to-steel contact rather than through the steel–composite interface. The interface is therefore subjected to substantially lower shear stresses than under the equivalent tensile load case. Second, the relatively low diameter-to-thickness ratio of the chord ($d/t \approx 14$) results in limited ovalisation of the chord section, which would otherwise generate the radial deformation pattern that drives debonding initiation at the saddle and crown regions. The combination of these two effects effectively suppresses the load transfer mechanism through the composite, and the joint response becomes governed by the steel section itself. The ductile response seen in the load–displacement curve is consistent with this interpretation, as it reflects yielding of the CHS outside the composite region rather than progressive interface damage.

It is important, however, to emphasise the conditions under which this behaviour was observed. The absence of debonding for the $-N_x$ + M_{op} load case is conditional on the geometric and material configuration tested in this study, in particular the brace-to-chord ratio $\beta = 1.0$, the low d/t ratio of approximately 14, and the wrapping geometry described in Section 2.1. For joints with thinner-walled chord sections, the increased chord ovalisation under compression and bending is expected to generate larger interface stresses, and debonding may then contribute to the response. Similarly, at lower β values the utilisation of the stiff chord walls is limited. The conclusion that $-N_x + M_{op}$ does not govern the joint performance should therefore not be generalised to thinner-walled or geometrically different composite joints without dedicated verification, and additional testing across a wider range of d/t and β values is recommended to establish the boundaries of this favourable behaviour.

3.5. Axial tension + in-plane bending loading

The load–deformation behaviour of the X-joint subjected to combined axial loading and in-plane bending, LC5 (N_x+M_{ip}), is analysed to assess the interaction effects between these two load components. The experimental load–deformation curves for this load case are presented in Fig. 18. Key stages in the deformation response are identified, corresponding to distinct changes in the load–displacement behaviour. While the axial response of the specimens remains consistent, greater variation is observed in the bending moment behaviour. This can be attributed to the role of the composite in resisting in-plane bending. Under this loading condition, the crown region—being more heavily loaded—is primarily governed by through-thickness behaviour of the laminate, involving combined Mode I and Mode II substrate debonding at the sharp corner of the thick composite. In contrast, the saddle region of the brace, which carries most of the tensile load, is more influenced by in-plane stresses. As a result, manufacturing variations—particularly in resin distribution—have a greater impact on the in-plane bending response, potentially explaining the differences observed between specimens. Nevertheless, the variation in maximum bending moment is limited to around 20%, which is relatively small given the typical variability in delamination resistance of composite laminates.

Initially, the joint loaded in combined axial tension and in-plane bending exhibits a linear elastic response up to point A. As the applied load increases, deviations from linearity emerge, indicating the onset of local debonding in the crown region. At point B, the first signs of debonding at the saddle position are detected through optical fibre measurements, as shown in Fig. 18c. The progression of debonding is marked by distinct points along the load–deformation curve C, D, and E each corresponding to major surface strain measurements captured by DIC, as illustrated in Fig. 19. The strain distribution at point D reveals that a larger portion of the brace circumference is utilized in the load transfer, aligning with the findings on welded joints reported by Hoadley et al. [15] for welded joints under this load condition.

The combination of axial loading and in-plane bending leads to a distinct load distribution between the crown and saddle regions. Debonding, most likely competing with local delaminations at the corner regions, has a more significant impact on the bending stiffness compared to the axial loading, as indicated by the greater debonding length in the crown region compared to the saddle region. Unlike the debonding progression observed in LC1 (N_x), LC2 (N_x + M_{op} (with M dominant)), and LC3 (N_x + M_{op} (with N dominant)), no distinct load drops are present in the load–displacement curves for this case. This suggests that debonding does not propagate from the saddle to the crown region. Instead, the stress distribution in this load combination starts to grow simultaneously, preventing the localised debonding progression in the saddle and crown regions as seen in the other load cases.

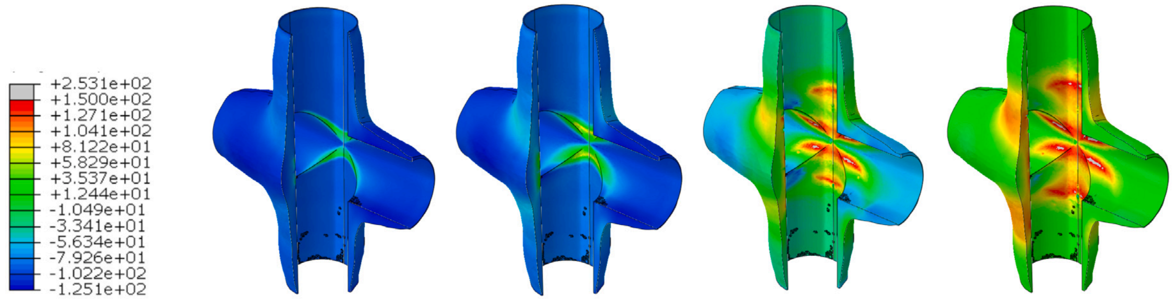

(a) Legend S11 (MPa) **(b)** Point A **(c)** Point B **(d)** Point C **(e)** Point D

Fig. 12. Longitudinal stress (along brace axis) distribution for load-case N_x for point A to D.

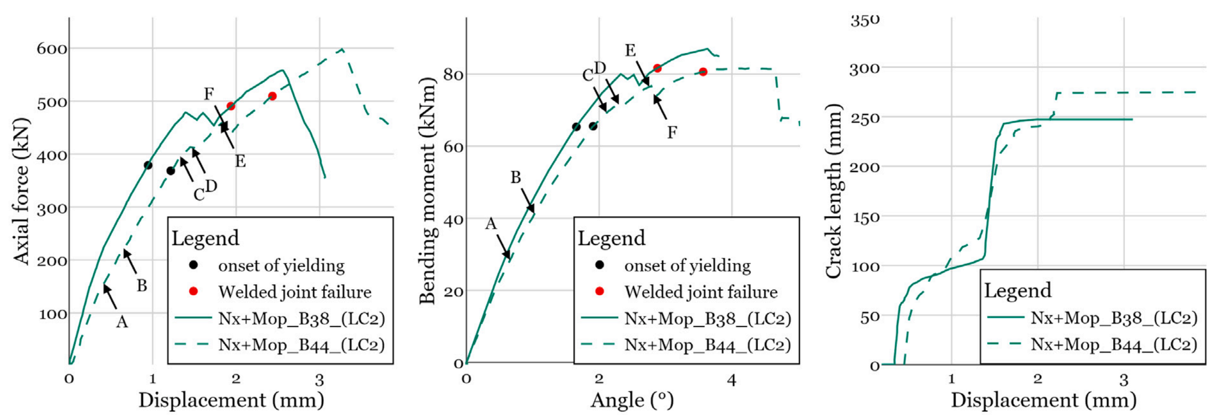

(a) Load displacement load case 2 **(b)** Moment angle load case 2 **(c)** Crack length load case 2

Fig. 13. Experimental results LC2 $N_x + M_{\mathrm{op}}$ (with M dominant).

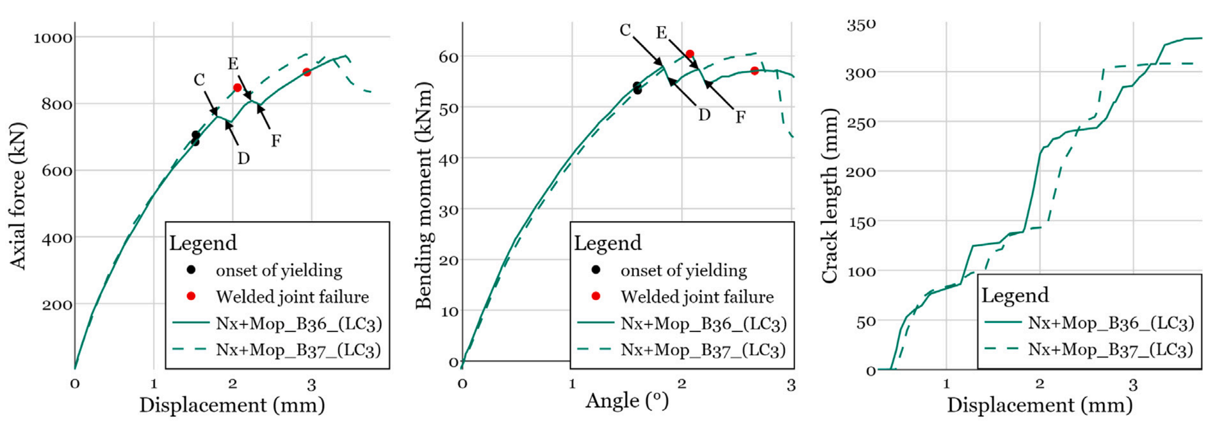

(a) Load displacement LC3 **(b)** Moment angle LC3 **(c)** Crack length LC3

Fig. 14. Experimental results LC3 $N_x + M_{\mathrm{op}}$ (with N dominant).

3.6. Axial tension + out-of-plane bending + in-plane bending loading

Two experiments were conducted to examine the full interaction between axial tension, out-of-plane bending, and in-plane bending. In addition to the conditions in LC3 and LC5, an additional rotational component was applied, resulting in loading ratios of $\frac{N}{M_{op}} = 12\ \mathrm{m}^{-1}$, $\frac{N}{M_{ip}} = 12\ \mathrm{m}^{-1}$. This setup was designed to assess the impact of combined bending on axial resistance and damage progression. The experimental results for this load case are presented in Fig. 20.

Similar to the other load cases, the joint response remains linear up to point A, after which initial brace substrate debonding is detected through optical fibre measurements. See Fig. 20(c). The load–deformation behaviour exhibits a two-stage progression, with a slower crack growth rate observed between points B and C/D, as well as between points D and E. During the first stage (B–C), both axial force and bending moment exhibit a steady increase. In the second stage (D–E), the increase is primarily attributed to axial loading, while the increase in bending moment resistance is less pronounced.

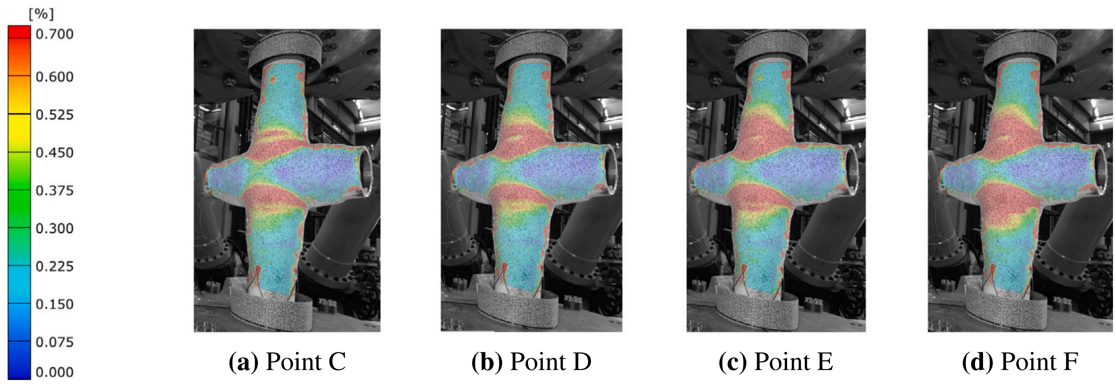

Fig. 15. Tensile major strain from DIC surface measurements of $N_x + M_{op}$ B36 (LC3) for point C to F.

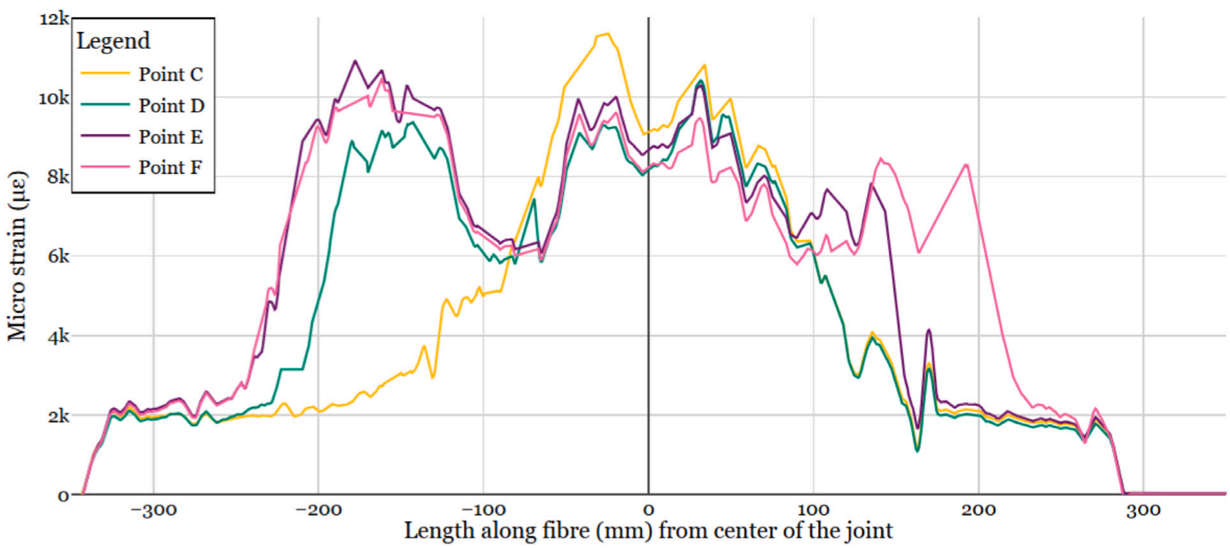

Fig. 16. Optical fibre strain measurements of $N_x + M_{op}$ B36 (LC3) at point C, D, E and F.

Major principal surface strain measurements obtained from DIC, shown in Fig. 21, indicate that substrate debonding primarily progresses in the axial load direction. Similar to $N_x + M_{ip}$, no significant drops in the load–deformation response are observed, suggesting that debonding between the crown and saddle regions occurs simultaneously. The results further show that in the initial stage, the bending stiffness for M_{op} and M_{ip} is comparable. However, as substrate debonding develops, the stiffness diverges, leading to a 5%–10% lower non-linear stiffness and bending resistance of M_{ip} compared to M_{op} bending as is observed in Fig. 20(b)

4. Comparison of load cases

4.1. Failure modes

Based on the experimental results, the load transfer mechanisms and failure modes for each loading condition are identified and presented in Fig. 22. Across all load cases, the dominant failure mechanism is either debonding at the steel-FRP interface or delamination within the composite near the interface. A distinction can be made between the primary and secondary interfaces, corresponding to the brace and chord surfaces, respectively [14]. The ductility of the joint is primarily governed by the failure of the primary interface. Final failure is characterised by a combination of complete substrate debonding on the tensile side and composite fracture at the edge of the delaminated region.

For combined loading cases, an interaction between debonding failure followed by composite failure is observed. This interaction arises because debonding propagation induces an interlocking effect of the steel brace within the composite, generating circumferential stresses in the composite. These stresses ultimately initiate a composite crack that propagates from the end of the composite towards the root of the joint after the debonding has fully progressed. The location and propagation direction of the composite crack vary depending on the bending moment direction.

For purely axial loading (N_x, LC1), failure is entirely governed by substrate debonding, culminating in complete debonding of the steel brace. Under combined axial and out-of-plane bending ($N_x + M_{op}$, LC2 and LC3), substrate debonding occurs on the tensile side of the brace. A similar failure pattern is observed for combined axial and in-plane bending (N_x+M_{ip}, LC5) and the fully combined loading case (N_x+M_{op}+M_{ip}, LC6), with the debonding area and composite fracture location aligning with the principal bending direction. However, crack merging between the crown and saddle regions is only observed for the axial (N_x) and axial + out-of-plane bending (N_x+M_{op}) load cases, suggesting that the stress redistribution promotes a continuous debonding path between these regions.

Findings indicate that the primary failure mode remains unchanged across all load cases, with ductility predominantly governed by substrate debonding or interface debonding of the brace section. The occurrence of composite fracture does not significantly enhance ductility but serves as a secondary failure mechanism. Notably, composite fracture only develops when substrate debonding is fully developed in regions subjected to tensile stress.

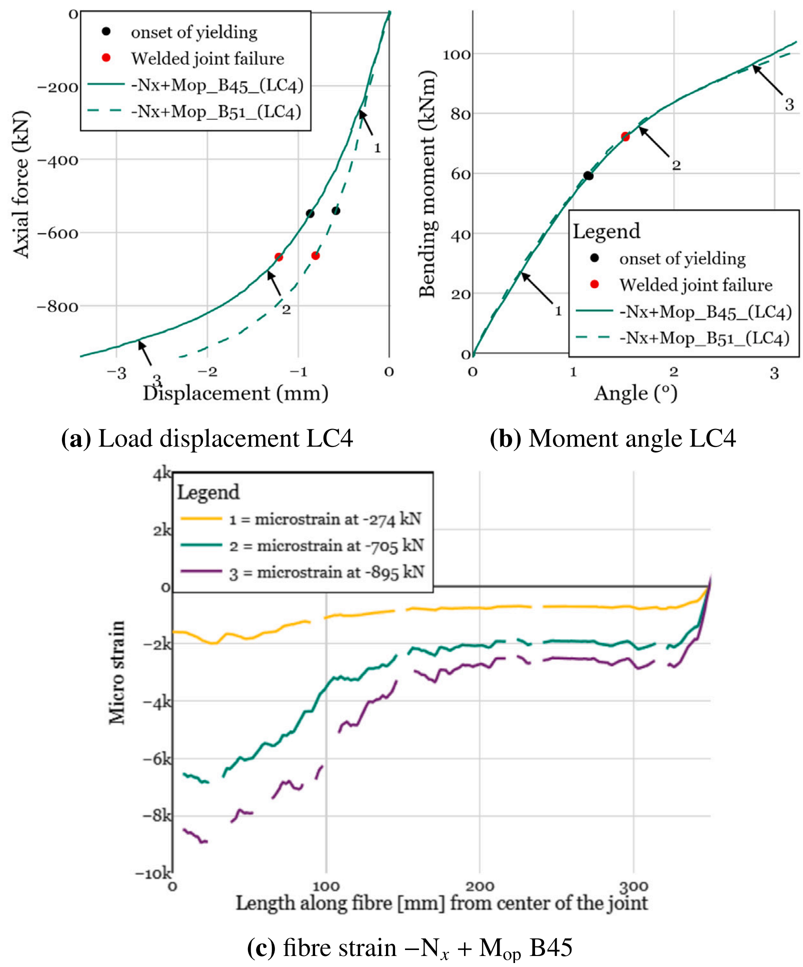

Fig. 17. Experimental results LC4.

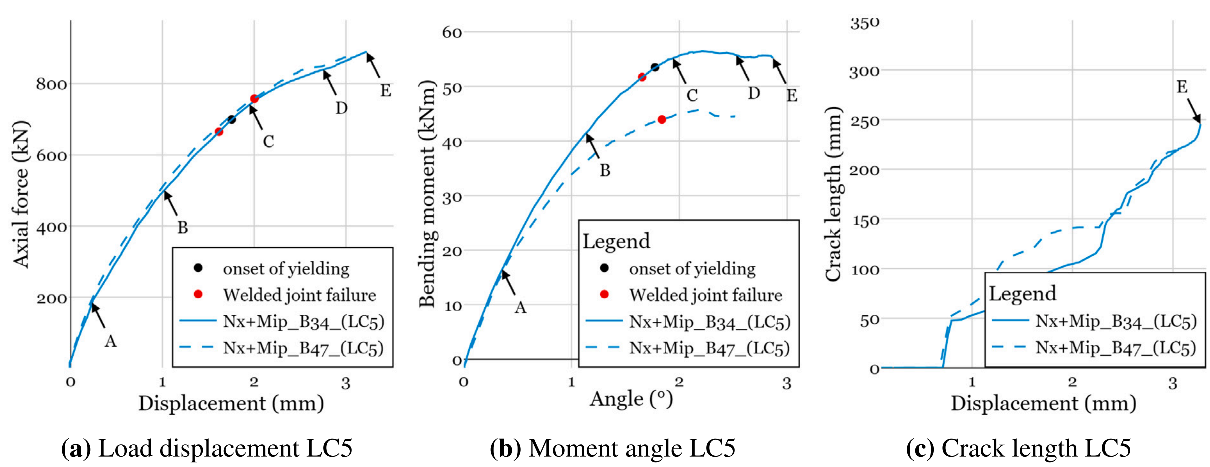

Fig. 18. Experimental results LC5 $N_x + M_{ip}$.

4.2. Load–deformation behaviour

As shown in Fig. 23, the initial axial and bending stiffness are practically independent of both the applied load case and the direction of the bending moment. While the onset of non-linearity exhibits slight variations depending on the axial force-to-bending moment ratio, the overall load–deformation response remains consistent across all load cases. The primary distinction lies in debonding crack progression: in purely axial and axial + out-of-plane bending load cases, crack merging between the crown and saddle regions leads to a sudden increase in crack length and noticeable discontinuities in the load–deformation curves, an effect not observed in other loading scenarios.

When comparing $N_x + M_{op}$ (LC3) and $N_x + M_{ip}$ (LC5), no significant difference is found in the interaction between axial and bending loading. This suggests that the direction of the bending moment does not significantly influence the combined resistance of the joint. Despite variations in substrate debonding progression, the ultimate resistance appears to be governed by the total delaminated area of the brace,

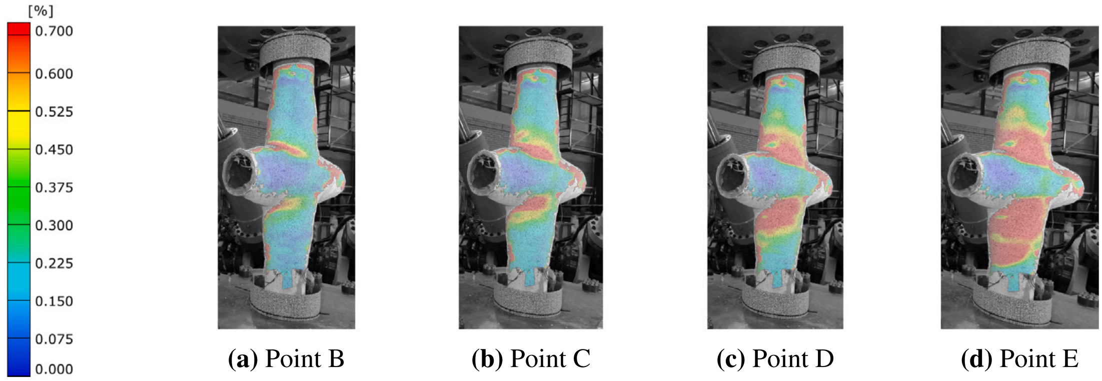

(a) Point B **(b)** Point C **(c)** Point D **(d)** Point E

Fig. 19. Major strain from DIC surface measurements at tensile side of $N_x + M_{ip}$ B34 (LC5) for point B to E.

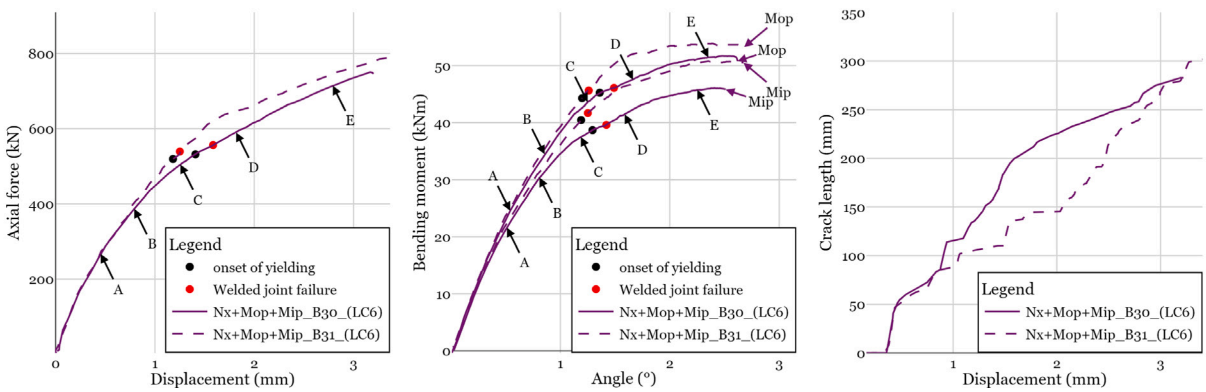

(a) Load displacement LC6 **(b)** Moment angle LC6 **(c)** Crack length LC6

Fig. 20. Experimental results LC6 $N_x + M_{op} + M_{ip}$.

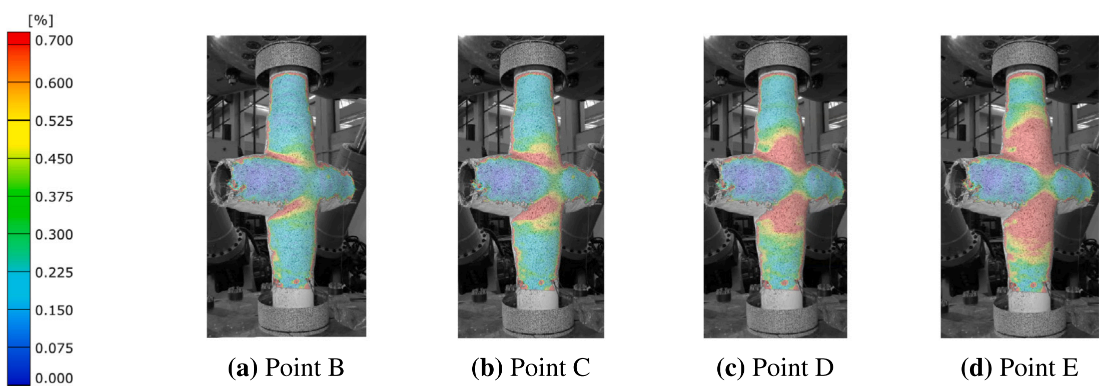

(a) Point B **(b)** Point C **(c)** Point D **(d)** Point E

Fig. 21. Tensile major strain from DIC surface measurements for $N_x + M_{op} + M_{ip}$ B30 (LC6) for point B to E.

which remains comparable between the two bending directions. However, a reduction in axial resistance is observed as the axial force-to-bending moment ratio decreases from 12 m^{-1} to 8.5 m^{-1}, indicating a dependency on the relative contribution of bending to the overall loading condition.

In addition to strength considerations, ductility plays a critical role in the structural performance of tubular joints. For steel CHS joints, Eurocode-based design practice typically requires that the ultimate limit load is reached before a deformation corresponding to 3% of the chord diameter (i.e., $3\% \times D \approx 5$ mm or about 5.7° of rotation). For all analysed load cases and the investigated composite joint geometry, this requirement is satisfied: the ultimate load is obtained prior to reaching the 3% deformation threshold. This observation is significant because it demonstrates that the composite tubular joint behaves within the desired ductile range, comparable to conventional welded CHS joints.

4.3. Interaction effects

Based on the experimental findings, an initial understanding of the load interaction effects on joint resistance can be established. As discussed previously, the direction of the applied bending moment does not appear to significantly influence the joint's ultimate resistance. This suggests that the interaction between the in-plane and out-of-plane bending moments follows a quadratic relationship, as expressed in Eq. (2).

To visualise this interaction, Fig. 24 presents the relationship between axial force and the total bending moment, incorporating the

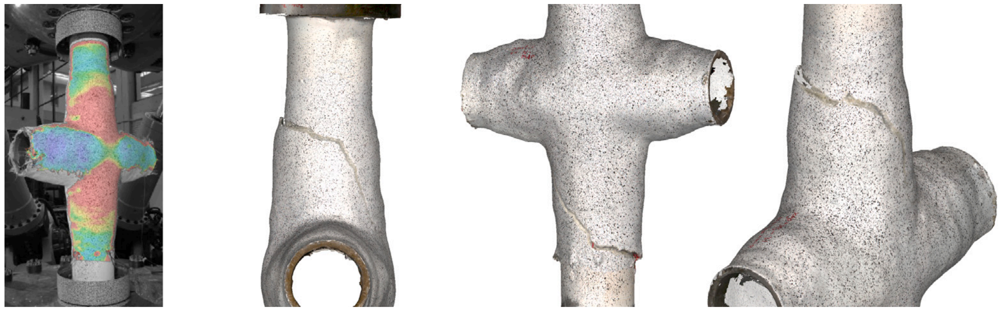

(a) LC1 **(b)** LC2 and LC3 **(c)** LC5 **(d)** LC6

Fig. 22. Failure modes.

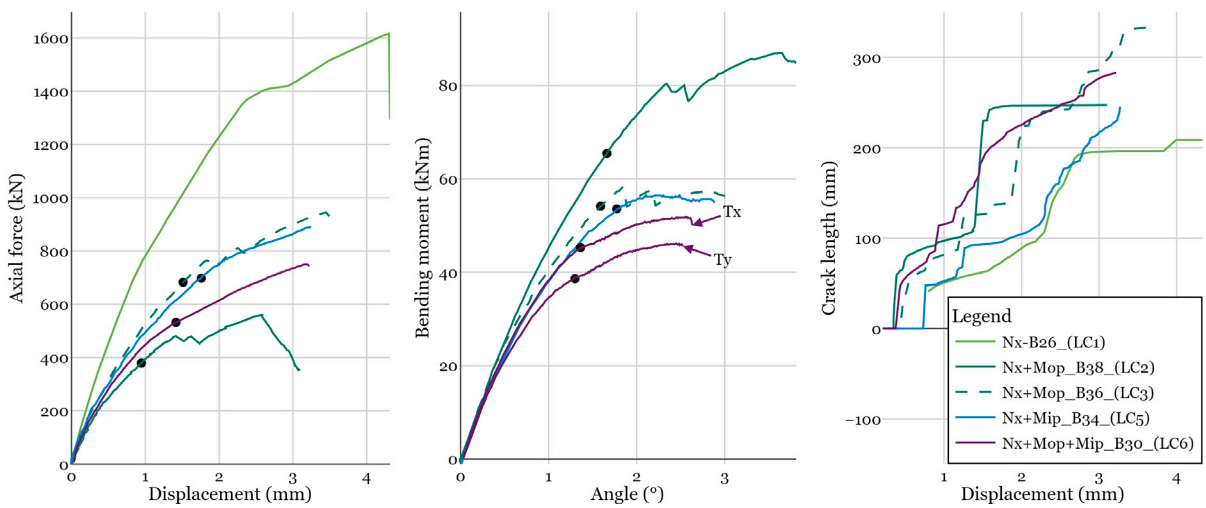

(a) Load displacement **(b)** Moment angle **(c)** Crack length

Fig. 23. Experimental results LC 2, 3, 5 and 6.

proposed interaction formulation. The results indicate that when a quadratic interaction is assumed between the bending moments, the $N_x + M_{op} + M_{ip}$ load case aligns well with the range of other biaxial loading conditions. This consistency further supports the validity of the proposed interaction model.

The exponents adopted in the proposed interaction equation are not only empirical fits to the experimental data, but can also be interpreted in terms of the underlying physical mechanisms governing debonding failure. Two observations form the basis of this interpretation.

The first concerns the quadratic interaction between the in-plane and out-of-plane bending moments. The wrapping geometry, measured from the chord face along the brace section, is rotationally uniform around the circumference of the brace. As a consequence, once the initial debonding front has developed, the brace responds in a similar manner regardless of the direction in which bending is applied: the resisting cross-section of the steel–composite interface presents the same stiffness and strength characteristics along any radial direction. The effective bending moment is therefore governed by the vectorial resultant of M_{op} and M_{ip}, which mathematically corresponds to the quadratic combination $\sqrt{(M_{op}/M_{op,u})^2 + (M_{ip}/M_{ip,u})^2}$.

The second concerns the linear interaction between axial force and the combined bending moment. At the steel–composite interface, debonding is driven primarily by Mode II (shear) strain, which arises from the shear stress transfer between the brace and the composite wrap. Under pure axial load, this Mode II strain is distributed approximately uniformly around the circumference of the brace. Under pure bending, it is distributed in a non-uniform pattern, concentrated on the tension side of the brace. When axial force and bending act simultaneously, the two strain contributions superpose directly at the interface; on the tension side, where debonding initiates, the total Mode II strain is the sum of the axial and bending contributions. Because debonding initiation is governed by the local strain reaching the critical interface value, a linear summation of the normalised axial and bending loads provides a physically consistent failure criterion. This linear interaction is also consistent with the behaviour reported for welded CHS X-joints with $\beta = 1.0$ under axial force and out-of-plane bending [15], suggesting that the linearity is not specific to the wrapped composite configuration but reflects a more general behaviour of combined loading in joints where the strain distribution is concentrated in the same location.

The proposed exponents ($\alpha = 1$ for axial force and $\beta = \gamma = 2$ within the quadratic bending interaction) are therefore not arbitrary calibrations: they follow from the rotational symmetry of the wrapping geometry and from the superposition of Mode II interface strains under combined loading. With respect to sensitivity, since the linearity originates from the strain-superposition argument and the quadratic combination from the rotational symmetry of the wrap, moderate variations in interface fracture toughness or composite material properties are expected to shift the magnitude of the uniaxial resistances N_{xu}, $M_{op,u}$ and $M_{ip,u}$ rather than the exponents themselves. This expectation is in line with the recent numerical parametric study of Cintra et al. [39], who showed for the same joint geometry that the interaction exponents vary by less than 2%–3% across a 40% variation in interface fracture toughness.

Table 4
Eq. (4) applied on experimental results.

Name	N_x (kN)	M_{op} (kN m)	M_{ip} (kN m)	Best fit	Eq. (4)	Failure mode
Nx+Mip B34	890	0	55	0.95	1.01	Root-to-brace-end debonding
Nx+Mip B47	878	0	44	0.85	0.91	Root-to-brace-end debonding
Nx+Mop B36	945	56	0	0.99	1.05	Root-to-brace-end debonding
Nx+Mop B37	950	57	0	1.00	1.06	Root-to-brace-end debonding
Nx+Mop B38	559	87	0	1.03	1.07	Root-to-brace-end debonding
Nx+Mop B44	601	81	0	1.00	1.05	Root-to-brace-end debonding
Nx+Mop+Mip B30	752	52	46	1.09	1.04	Root-to-brace-end debonding
Nx+Mop+Mip B31	791	53	50	1.15	1.10	Root-to-brace-end debonding

Building on these observed interaction effects, an interaction criterion for tubular composite joints is proposed in Eq. (3), in a similar form as interaction criterion for welded CHS joints as given in; Eurocode [19], DNV [20], NORSOK [21], and CIDECT [22]. The interaction parameters α, β, γ, and ζ are determined by calibrating the model against experimental data. The uniaxial bending resistance for both in-plane and out-of-plane bending is absent. When such detailed data is not available, an initial estimate can be made by assuming that the plastic bending moment represents the ultimate bending resistance. Based on this assumption, the best-fit exponents are: $\alpha = 1$, $\beta = 1.4$, $\gamma = 1.4$, $\zeta = 0.85$. These values result in an average unity check of 1.0.

The variability of the load combinations was assessed using the complete experimental dataset. The corresponding standard deviations are:$N_x + M_{ip} = 5\%$, $N_x + M_{op} = 1\%$, $N_x + M_{op} + M_{ip} = 3\%$.

A more engineering fit with 10% conservative prediction is found for debonding failure of tubular composite joints using $\alpha = 1$, $\beta = 2$, $\gamma = 2$, and $\zeta = 0.5$, as shown in Table 4. Resulting in the interaction formulation presented in Eq. (4). See Fig. 24. It is intended to be used as a complement to existing CHS design frameworks such as EN 1993-1-8 [19], DNV-ST-0126 [20], NORSOK N-004 [21], and the CIDECT design guide [22]. For a tubular composite joint design, the designer first determines the uniaxial design resistances related to debonding failure of the brace section, N_{xu}, M_{opu}, and M_{ipu}, from dedicated finite element models of the joint. The action effects $N_{x,Ed}$, $M_{op,Ed}$, and $M_{ip,Ed}$, obtained from the global jacket analysis under the governing load combinations, are then substituted into Eq. (4), allowing each load combination from the jacket design to be verified analytically through a single unity check, without the need for additional joint-level FE analyses per load case. The joint is considered adequate when the left-hand side of Eq. (4) does not exceed unity. The equation is calibrated for the geometric and material configuration tested in this study, where debonding governs failure. Application of this criterion outside the calibrated range — in particular for different steel and composite thicknesses — requires additional experimental validation.

$$M_{res} = \sqrt{\left(\frac{M_{op}}{M_{op_u}}\right)^2 + \left(\frac{M_{ip}}{M_{ip_u}}\right)^2} \tag{2}$$

$$\left(\frac{N_x}{N_{x_u}}\right)^\alpha + \left(\left(\frac{M_{op}}{M_{op_u}}\right)^\beta + \left(\frac{M_{ip}}{M_{ip_u}}\right)^\gamma\right)^\zeta = 1 \tag{3}$$

$$\frac{N_x}{N_{x_u}} + \sqrt{\left(\frac{M_{op}}{M_{op_u}}\right)^2 + \left(\frac{M_{ip}}{M_{ip_u}}\right)^2} = 1 \tag{4}$$

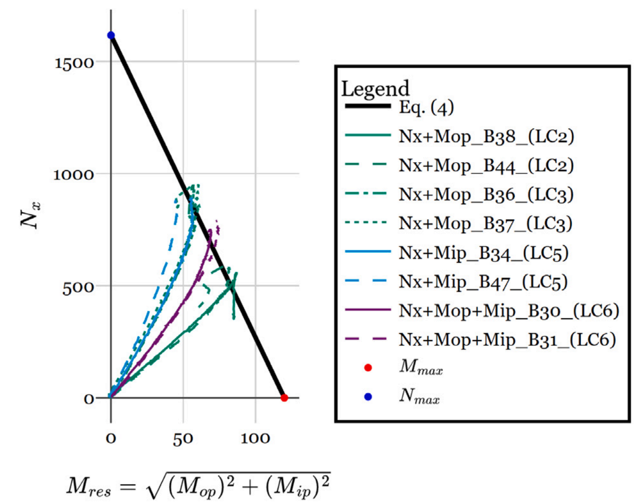

Fig. 24. Axial load vs. total bending moment.

5. Conclusions

The experimental investigation of medium-scale 90° tubular composite X-joints, featuring CHS members with a diameter of ø168.3 × 12.5 mm, subjected to six distinct loading conditions, has yielded key insights into the load transfer mechanisms, failure modes, and failure progression. The use of the Hexapod apparatus [23] enabled precise application of proportional combined axial and bending loads, facilitating a controlled study of multi-axial loading effects. Across all load cases, the dominant failure mode was identified as substrate debonding or interface debonding, with ductility primarily governed by the failure of this interface. This outcome was not incidental but deliberately targeted: both the composite and steel tubes were intentionally made thicker to suppress other failure modes and promote interfacial debonding. This design choice enabled controlled observation of the interface behaviour, allowing the study to successfully isolate and characterise the failure mechanism and establish a corresponding failure criterion for interface debonding. Debonding was fully developed under tensile stress before any composite fracture occurred, and while composite failure was observed in specific load cases, it did not contribute significantly to ductility. The failure mechanisms and their progression were systematically captured and quantified using 3D Digital Image Correlation (DIC) and distributed optical fibre sensing.

Key findings of the study include:

1. Across all load cases, the tubular composite X-joints consistently exhibited debonding at or near the steel–composite interface as the governing failure mechanism. Crack initiation always originated at the brace root and advanced towards the end of the composite wrap, with the propagation path dependent on the applied load. N_x, and $N_x + M_{op}$, produced localised debonding that rapidly merged between the crown and saddle regions, whereas $N_x + M_{ip}$ and $N_x + M_{op} + M_{ip}$ resulted in a more uniform circumferential debonding pattern. Despite variations in loading complexity, the failure process remained Mode-II-dominated, with stable interface failure observed in all load cases.
2. The interaction between axial force and bending is well represented by a linear–quadratic formulation: bending moments about the two principal axes interact quadratically, while their combined action with axial force remains almost linear. This

interaction criterion captures the underlying debonding-driven failure behaviour across all combined load cases with a conservatism of roughly 10%, offering a practical and robust design tool for tubular composite joints.

3. Bending resistance is independent of direction: the ultimate bending moment was not influenced by whether bending occurred in-plane or out-of-plane, as resistance was governed by substrate debonding in the brace section, an direction-insensitive mechanism. This leads naturally to a quadratic interaction between M_{op} and M_{ip}.
4. Initial stiffness is load-case invariant: both the axial and bending stiffnesses were shown to be insensitive to the specific loading configuration or the direction of bending, confirming that the early-stage response is dominated by the intact composite–steel interface rather than by load-path complexity.
5. All load conditions exhibited sufficient ductile behaviour: the monotonic load–deformation curves consistently showed that the ultimate load was reached before the 3% deformation criterion (≈5 mm displacement, ≈5.7° rotation) was exceeded. Ultimate rotations of approximately 2°–3° were achieved under combined loading, well within the deformation limit, confirming the favourable structural behaviour of the tubular composite joint.
6. Bending-induced debonding produces secondary composite cracking: in load cases involving bending, debonding progression caused interlocking between the steel brace and composite wrap, generating circumferential stresses that triggered composite cracking whose location and direction depended strongly on the bending moment orientation.

Overall, the results demonstrate that while combined loading influences the sequence and extent of crack propagation, it does not alter the primary failure mechanism. These findings provide valuable insights for the structural design and optimisation of tubular composite joints subjected to complex loading conditions, enhancing the understanding of their failure behaviour and ductility characteristics.

CRediT authorship contribution statement

Mathieu Koetsier: Writing – original draft, Visualization, Validation, Methodology, Investigation, Formal analysis, Data curation. **Gisele Cintra:** Writing – review & editing, Validation, Investigation, Formal analysis. **Marko Pavlovic:** Writing – review & editing, Supervision, Project administration, Methodology, Funding acquisition, Conceptualization.

Declaration of generative AI and AI-assisted technologies in the manuscript preparation process.

During the preparation of this work, the authors used ChatGPT to improve readability and language. After using this tool, the authors reviewed and edited the contents as needed, and take full responsibility for the contents of the paper.

Declaration of competing interest

The authors declare that they have no known competing financial interests or personal relationships that could have appeared to influence the work reported in this paper.

Acknowledgements

The authors would like to express their gratitude to RVO for the financial support with Topsector Energiesubsidie van het Ministerie van Economische Zaken through WrapNode-I and WrapNode-II project, and Tree Composites B.V. for the production of specimens.

Data availability

Data will be made available on request.

References

[1] Wardenier J, Packer JA, Zhao X-L, der Vegte GJ. Hollow sections in structural applications. Rotterdam, The Netherlands: Bouwen met staal; 2002.
[2] Siriwardane SC, Adasooriya ND, Pavlou D. Fatigue strength curve for tubular joints of offshore structures under dynamic loading. Dynamics 2021;1(1):125–33. http://dx.doi.org/10.3390/dynamics1010007, URL https://www.mdpi.com/2673-8716/1/1/7.
[3] Lesani M, Bahaari MR, Shokrieh MM. FRP wrapping for the rehabilitation of Circular Hollow Section (CHS) tubular steel connections. Thin-Walled Struct 2015;90:216–34. http://dx.doi.org/10.1016/j.tws.2014.12.013.
[4] Fu Y, Tong L, He L, Zhao XL. Experimental and numerical investigation on behavior of CFRP-strengthened circular hollow section gap K-joints. Thin-Walled Struct 2016;102:80–97. http://dx.doi.org/10.1016/j.tws.2016.01.020.
[5] Nassiraei H, Rezadoost P. Stress concentration factors in tubular T/Y-joints strengthened with FRP subjected to compressive load in offshore structures. Int J Fatigue 2020;140. http://dx.doi.org/10.1016/j.ijfatigue.2020.105719.
[6] Sandal K, Verbart A, Stolpe M. Conceptual jacket design by structural optimization. Wind Energy 2018;21(12):1423–34. http://dx.doi.org/10.1002/we.2264.
[7] Lesani M, Bahaari MR, Shokrieh MM. Numerical investigation of FRP-strengthened tubular T-joints under axial compressive loads. Compos Struct 2013;100:71–8. http://dx.doi.org/10.1016/J.COMPSTRUCT.2012.12.020.
[8] Lesani M, Bahaari MR, Shokrieh MM. Experimental investigation of FRP-strengthened tubular T-joints under axial compressive loads. Constr Build Mater 2014;53:243–52. http://dx.doi.org/10.1016/j.conbuildmat.2013.11.097.
[9] Sadat Hosseini A, Bahaari MR, Lesani M. Parametric study of FRP strengthening on stress concentration factors in an offshore tubular T-joint subjected to in-plane and out-of-plane bending moments. Int J Steel Struct 2019;19(6):1755–66. http://dx.doi.org/10.1007/S13296-019-00244-0.
[10] Hosseini AS, Bahaari MR, Lesani M. SCF distribution in FRP-strengthened tubular T-joints under brace axial loading. Sci Iran 2020;27(3 A):1113–29. http://dx.doi.org/10.24200/SCI.2018.5471.1293.
[11] Pavlovic M, Bogers P, Veljkovic M. Method for making a virgin joint between two separate structural hollow sections, and such a virgin joint. 2023.
[12] Feng W, Pavlovic M. Fatigue behaviour of non-welded wrapped composite joints for steel hollow sections in axial load experiments. Eng Struct 2021;249:113369. http://dx.doi.org/10.1016/J.ENGSTRUCT.2021.113369.
[13] Koetsier M, Mylonopoulos V, Wolters M, Pavlović M. Comparative analysis of non-welded wrapped composite joints versus welded joints under multi-axial load conditions in offshore wind turbine supporting structures: A fatigue performance evaluation. In: ASME 2024 43rd international conference on ocean, offshore and arctic engineering. International conference on offshore mechanics and arctic engineering, vol. 7, Singapore: ASME; 2024, V007T09A020. http://dx.doi.org/10.1115/OMAE2024-124828.
[14] He P, Pavlovic M. Failure modes of bonded wrapped composite joints for steel circular hollow sections in ultimate load experiments. Eng Struct 2022;254:113799. http://dx.doi.org/10.1016/J.ENGSTRUCT.2021.113799.
[15] Hoadley P, U C, Yura J. Ultimate strength of tubular joints subjected to combined loads. In: Offshore technology conference. Vol. OTC 4854, 1985, URL http://onepetro.org/OTCONF/proceedings-pdf/85OTC/All-85OTC/OTC-4854-MS/2077377/otc-4854-ms.pdf/1.
[16] Hoadley PW, Yura JA. PMFSEL report 83-3 ultimate strength of tubular joints subjected to combined loads. Tech. rep., Austin Texas: University of Texas at Austin; 1983.
[17] Makino Y, Kurobane Y, Takizawa S, Yamamoto N. Behavior of tubular T- and K-joints under combined loads. Offshore Technol Conf 1986;OTC–5133–MS. http://dx.doi.org/10.4043/5133-MS.
[18] Swensson KD, Yura JA. PMFSEL report 86-3. Tech. rep., Austin Texas: University of Texas at Austin; 1986.
[19] Standardization ECF. NEN-EN 1993-1-8 Eurocode 3: Design of steel structures - Part 1-8: Design of joints. Brussels, Belgium: CEN; 2011.
[20] Veritas DN. DNVGL-ST-0126: Support structures for wind turbines. Høvik, Norway: DNV GL; 2021.
[21] Norwegian Technology Standards Institution. NORSOK standard N-004 design of steel structures. Oslo: Norwegian Technology Standards Institution; 1998.
[22] Wardenier J, Kurobane Y, Packer J, Vegte Gvd, Zhao X-L. Design guide for circular hollow section (CHS) joints under predominantly static loading. Geneva, Switzerland: CIDECT; 2008, http://dx.doi.org/10.1680/dofrcs.64447.205.
[23] Delft University of Technology. Hexapod. 2018, Hexapod experimental platform for offshore structure testing. URL https://www.tudelft.nl/me/over/afdelingen/maritime-and-transport-technology/research/ship-and-offshore-structures/facilities/hexapod.

[24] Koetsier M, Moreira MA, Wolters M, Pavlović M. Lifetime prediction of Tubular Composite Joints through multi-axial fatigue load experiments and VCCT. Eng Struct 2026;358:122623. http://dx.doi.org/10.1016/j.engstruct.2026.122623.

[25] Koetsier M, Yang J, Wolters M, Pavlovic M. Experimental investigation of wrapped composite X-joints under monotonic uniaxial and multi-axial load conditions. 2023, http://dx.doi.org/10.5281/zenodo.8070753.

[26] Bufalari G. On multiaxial fatigue of welded joints in steel maritime structures: Strength and mechanism contributions (Ph.D. thesis), Delft University of Technology; 2024, http://dx.doi.org/10.4233/uuid:0e252a85-d420-48ef-b74e-3c2c9751fa27.

[27] GmbH CZGM. ARAMIS adjustable. 2023, URL https://www.gom.com/en/products/3d-testing/aramis-adjustable.

[28] Incorporated LI. ODISI 6000 optical sensor interrogation system. 2023, URL https://lunainc.com/products/odisi-6000-optical-sensor-interrogation-system.

[29] Koetsier M, Pavlovic M. Crack propagation quantification in fibre-reinforced polymer composites through distributed optical fibre sensing. In: 21st European conference on composite materials. The European Society for Composite Materials (ESCM) and the Ecole Centrale˜...; 2024, p. 198–205.

[30] Feng W, Pavlovic M, Koetsier M, Veljkovic M. Interfacial fatigue debonding retardation in wrapped composite joints: Experimental and numerical study. Compos Struct 2023;319:117146. http://dx.doi.org/10.1016/J.COMPSTRUCT.2023.117146, URL https://www.sciencedirect.com/science/article/pii/S0263822323004907#f0060.

[31] Artec3d. Artec Leo. 2022, URL https://cdn.artec3d.com/pdf/Artec3D-Leo.pdf.

[32] He P, Wolters M, Waltener C, Pavlovic M. Debonding behavior of non-welded wrapped composite X-joints subjected to monotonic tensile load – Numerical study and validation. Eng Struct 2024;321(September):118969. http://dx.doi.org/10.1016/j.engstruct.2024.118969.

[33] Corp. DSS. Abaqus unified FEA - SIMULIA. 2023.

[34] He P. Debonding resistance of CHS wrapped composite x-joints (Ph.D. thesis), Delft University of Technology; 2023, http://dx.doi.org/10.4233/UUID:3AD94EE9-07FD-47F9-A766-843A91830534, URL https://repository.tudelft.nl/islandora/object/uuid%3A3ad94ee9-07fd-47f9-a766-843a91830534.

[35] Ametek C. VXelements acquisition modules for 3d scanning devices. 2022, URL https://www.creaform3d.com/en/products/software/vx-elements.

[36] Autodesk Inc. Autodesk inventor 2024. 2024.

[37] Yang J, Arouche MM, Egilsson S, Koetsier M, Peeters T, Pavlovic M. Size effects on mode I and mode II fracture behavior of FRP–steel bonded interface: Experimental and numerical investigation. J Compos Constr 2025;29(2):4025006. http://dx.doi.org/10.1061/JCCOF2.CCENG-4760, URL https://ascelibrary.org/doi/abs/10.1061/JCCOF2.CCENG-4760.

[38] Yang J, Koetsier M, Peeters T, Wolter M, Pavlovic M. Size effects on the structural behaviour of wrapped composite CHS joints. Ce/Papers 2023;6(3–4):297–301. http://dx.doi.org/10.1002/cepa.2649, URL https://onlinelibrary.wiley.com/doi/abs/10.1002/cepa.2649.

[39] Cintra G, Koetsier M, Mylonopoulos V, Pavlovic M. Influence of fracture toughness on multi-axial loading interaction criteria for wrapped composite X-joints. Thin-Walled Struct 2026;228:115143. http://dx.doi.org/10.1016/J.TWS.2026.115143, URL https://linkinghub.elsevier.com/retrieve/pii/S0263823126006671.